Rock Mechanics and Rock Engineering (2026) 59:2395–2414
https://doi.org/10.1007/s00603-025-04902-0

ORIGINAL PAPER

Application of a Hierarchical Solution Scheme to the Analysis and Design of Large-Scale Tabular Mine Layouts

J. A. L. Napier[1] · D. F. Malan[1] · Y. Jooste[2]

Received: 23 April 2025 / Accepted: 24 August 2025 / Published online: 10 September 2025

Abstract

This paper outlines a hierarchical computational strategy for solving large-scale tabular deposits using the displacement discontinuity boundary element method. This scheme facilitates the detailed analysis of local regions of interest, where current mining activity is in progress. The suggested approach requires an overall solution of the mine layout with a coarse element mesh to be obtained, which is then used to generate the background stress field for fine-scale solutions in selected regions of interest. The fine mesh solutions are established using the appropriate induced external coarse solution stress influence calculated in the selected region of interest using high order elements. The fine-scale solutions may involve detailed excavation extensions or time-dependent crushing of the fracture zone adjacent to the mined excavation edges. This analysis may require periodic re-calculation of the coarse scale background influence. An additional influence matrix partitioning scheme is also proposed as a strategy to incorporate automatically the effect of the induced background stress influence. A case study simulating the time-dependent convergence of a mining panel in a large-scale shaft pillar geometry is used to illustrate these hierarchical solution schemes.

Highlights

- This paper illustrates a hierarchical computational strategy for solving large-scale tabular layouts using the displacement discontinuity boundary element method. Particular attention is given to addressing the accuracy of the scale transition between coarse and fine mesh calculations using high order elements.
- The beneficial use of influence matrix partitioning in local regions of interest allows an efficient analysis of the time-dependent evolution of the fracture zone for stability modelling and the assessment of adverse ground conditions, where current mining activity is in progress.
- A simulation of the time-dependent convergence of a mining panel in a large-scale shaft pillar geometry is presented to illustrate the application of the proposed procedure.
- Time-dependent convergence profiles similar to those recorded in underground panels can be simulated.

Keywords Tabular stope · Displacement discontinuity modelling · Multi-scale solution · Stope convergence

1 Introduction

The planning of late-life extraction sequences in deep-level tabular mines presents a number of computational difficulties. These tabular geometries are commonly found in the gold mines of South Africa (e.g., McGarr and Wiebols 1977; Gay 1979; Napier and Malan 2018; Jooste et al. 2023). In many of the mature gold mines, remnants are extracted (Jooste and Malan 2020). There is a need to determine the stress induced by extensive historically mined-out regions

✉ D. F. Malan
francois.malan@up.ac.za

[1] Department of Mining Engineering, University of Pretoria, Pretoria, South Africa

[2] Harmony Gold Mining Company Limited, Randfontein, South Africa

on the current areas of mining activity. The panel roof to floor convergence changes must also be estimated as mining progresses to design rockburst-resistant support (Malan and Napier 2018b). It is generally unclear whether time-dependent settlement in these remote mined regions will have returned the stress state to the original primitive stress field values. If this is not the case, it is necessary to include the previously mined-out regions in the calculation of induced stress values in the crush zone ahead of currently active mining panels in small-scale regions of interest.

The combination of a very large tabular mining area with irregular layouts, the small face advance increments and the possible generation of stress in the back areas of the old stopes presents a formidable problem to solve using numerical modelling. The motivation for using the displacement discontinuity technique is that a large mining area with a complex geometrical outline which contains irregular remnant areas can be relatively easily simulated. The remnant shapes are often highly irregular owing to different historical mining directions and panels are frequently abandoned for various reasons. These large-scale tabular geometries are exceedingly difficult to solve using three dimensional finite difference or finite element grids. For example, when simulating tabular coal mine problems, Adhikary et al. (2016) noted that owing to the complexity of the geometries and the long computational times, researchers generally resort to two-dimensional section simulations. In contrast, it is feasible to simulate the entire geometry shown in Fig. 1, and even much larger, using displacement discontinuity codes. A number of finite difference codes are available, such as the suite of programs known as FLAC3D, developed originally by Cundall (see, for example, Cundall 1987). An early example of a displacement discontinuity code to solve tabular excavation problems was developed at the South African Chamber of Mines Research Organisation by Deist et al (1972) and called MINSIM (Mining Simulator). Other displacement discontinuity codes are presented in the book of Crouch and Starfield (1983) and more recent developments of the tabular excavation analysis code (TEXAN) is described by Napier and Malan (2007). A popular general purpose boundary element program called MAP3D has been developed by Wiles (2005). As a further motivation for the use of the displacement discontinuity method in this paper, it should be noted that finite element and finite difference modelling of large-scale tabular excavations can become extremely cumbersome if the solution mesh is required to cover a very large region surrounding the extensive reef plane excavations. As an example, Fuławka et al. (2025) presented large-scale 3D numerical simulations of a room and pillar copper mine in Poland using the finite element method (GTS NX software). The model was large with a plan projection of 2000 m × 2000 m. The pillar and overall layout geometries were restricted to rectangular shapes and it is doubtful if irregular layout geometries can be easily generated. In comparison, if the background region can be considered to be a uniform elastic material the boundary element technique provides an elegant approach in which the solution mesh is confined to the description of the excavation surfaces. In addition, the TEXAN code employs existing techniques developed by the authors (see, e.g., Malan and Napier 2018a, b; Napier and Malan 2018) for the resolution of tabular mine excavation face crushing and time-dependent failure analysis, which are not available in general commercial codes such as Map3D.

An example of the problem described is presented in Fig. 1. This is the plan view of part of a mine showing the tabular stopes and a remnant that was left in the centre of the excavation. The active mining panels are shown and four of these panels are being mined in the remnant. The typical mining height for these stopes is 1.6 m (Fig. 2). The average face advance is approximately 1 m per blast, and the face length of the active mining panels is approximately 30 m.

A further layout example is illustrated in Fig. 3. In the deeper modern gold mines, scattered mining with dip pillars has replaced the traditional longwall mining method and has been found to minimise the levels of stress induced seismic activity by restricting the overall volumetric stope convergence. The simulation of total back area closure is important in assessing the overall re-distribution of stress as the mined area is increased. The modelling total closure state does require special attention. This has been addressed by attempts to replicate the effective bulking of the rock mass in the back areas as described by Jooste et al (2023).

The modelling problem is again presented as a large area that needs to be simulated, although specific areas of interest may, for example, comprise a small localised region or a single 30 m panel that has been instrumented to obtain convergence data for improved support designs. Furthermore, when studying the effect of mining rate (Napier and Malan 2018), small face advance increments of approximately 1 m need to be simulated with some precision within a very large regional model that extends over hundreds of metres along both strike and dip directions.

The main computational challenge in the analysis of the problems described here is to incorporate the effects of remote mining while performing a fine scale analysis of the time-dependent fracture zone evolution in a limited area of interest. This paper proposes a formal protocol to achieve this using coarse and fine mesh schemes in the appropriate regions. To implement this scheme it is important to implement an accurate transition mechanism at the interfaces between different mesh sizes. It is shown that this can be addressed conveniently using high order element representations at the coarse scale to achieve a smooth solution transition at the interface. In addition to this attention is given to the efficient calculation of multiple time-step calculations at the fine scale by employing

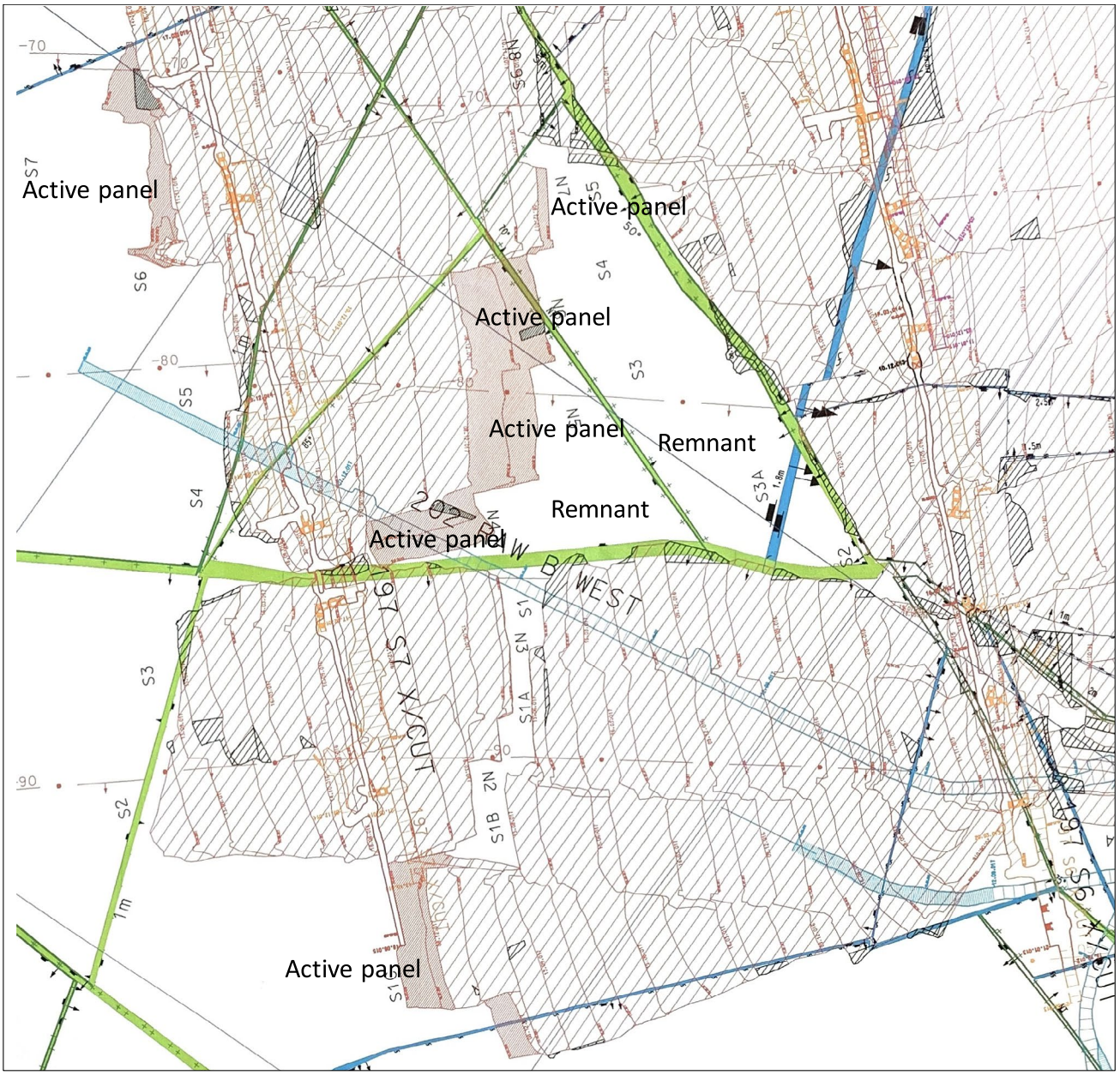

Fig. 1 Complex mining geometry typically found in the mature deep tabular gold mines in South Africa. This illustrates a plan view of the tabular layout and the dimensions of the area shown are 300 m × 290 m. The white blocks are unmined portions of the reef

both high order element schemes and by introducing an influence matrix partitioning scheme. It is demonstrated that this can improve the fine scale numerical performance significantly enabling the evaluation of multiple time step increments in the defined local regions of interest.

Fig. 2 Typical conditions in the face area of a deep tabular stope with the gold reef shown on the left. The centre gully of the stope is on the right. The dip of the reef can be seen on the left and is approximately 25°

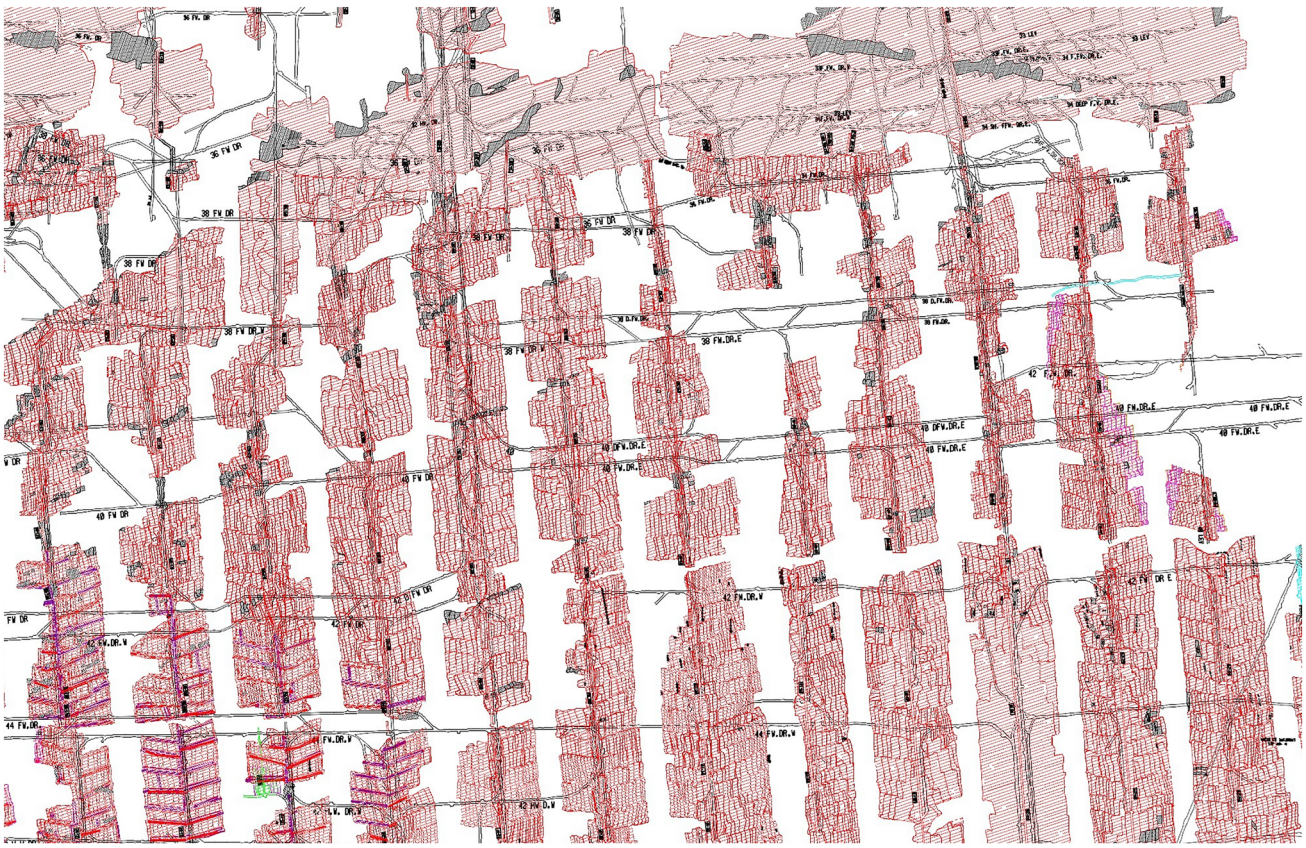

Fig. 3 Plan view of a modern dip pillar layout in the deep tabular gold mine stopes. The size of the mining area shown in the diagram is approximately 2.2 km × 1.4 km. The reef dip is approximately 30° to the bottom of the figure. Note the older longwall mining method at the top of the figure

2 Summary of the Displacement Discontinuity Solution of Tabular Mine Excavations

The analysis of the stress and convergence distribution in large-scale tabular mining layouts has been a problem of significant international interest in the mining industry for many decades. The application of the displacement discontinuity boundary element method to tabular mining problems can be traced to pioneering developments in the United Kingdom for the design of coal mines (see Berry and Sales 1962), where the essential assumption is made that the mining height can be neglected and each excavation is approximated as a slit or crack surface in the rock mass. The method was introduced subsequently by Salamon (1963) in South Africa as the so-called "Face Element Principle" for the analysis of tabular coal and gold mine layouts. Some early examples of the initial digital computer codes that were developed for the calculation of deep level tabular mine layout elastic convergence and stress distributions are described by Plewman et al. (1969), Deist et al. (1972) and Crouch and Starfield (1983). The displacement discontinuity method is useful as well to model slip on fault surfaces. An early examples of attempts to carry this out using displacement discontinuity methods are described by Ryder (1988).

The determination of ride and convergence movements in tabular excavations using the displacement discontinuity boundary element method requires the excavation to be tessellated using a triangular or quadrilateral element mesh. The unknown displacement discontinuity vector distribution within each element is assumed to be defined at one or more designated collocation point positions. The relationship between the traction vectors and the displacement discontinuity vectors for all collocation points covering all elements can be assembled compactly as a matrix equation of the form:

$$T = KD + E \tag{1}$$

The column vectors T and D in Eq. (1) represent all the individual traction and displacement discontinuity components at each collocation point in the defined solution space. For a problem comprising N collocation points, vectors T and D will, therefore, each have $3N$ entries representing the individual vector components $T_x(P), T_y(P), T_z(P)$ and $D_x(Q)$, $D_y(Q)$, $D_z(Q)$ at each "receiving" collocation point P and "sending" collocation point Q. The vectors T and D are expressed in local receiving and sending element coordinate systems, respectively. The vector E with $3N$ entries represents the field stress and any additional "external" traction vector components at all "receiving" points P.

The $3N \times 3N$ influence matrix K cells must be evaluated for each receiving and sending collocation point pair. The matrix entries are determined by integrating assigned shape function distributions for the displacement discontinuity vector components at each collocation point within each element (see, for example, Crouch and Starfield 1983; Napier and Malan 2007). The local traction vector components at all points P of an open excavation are zero but within the excavation edge crush zones or in regions, where total roof to floor closure occurs, there will generally be a non-linear relationship between the value of the local traction vector and the corresponding local displacement discontinuity vector. The treatment of such behaviour can be carried out readily when using an iterative solution of the equation system. The solution to Eq. (1) can be determined by direct inversion of the influence matrix K in small-scale problems with explicit traction boundary conditions or, more generally, must be obtained using an iterative solution procedure (Napier and Malan 2007). Symbolically, Eq. (1) can be written as an implicit relationship of the form $T(D) = KD + E$ for the unknown displacement discontinuity vector D at each collocation point which can be refined in successive iterative cycles to determine the value of D.

The main computational cost incurred in the solution of large-scale layout problems is the efficient determination of the influence function values and the implementation of robust iterative techniques to resolve nonlinear boundary relations that arise between specific traction components in cases of friction sliding on faults or the treatment of inelastic effects between the opposing roof and floor surfaces of each discontinuity collocation point. These problems have been recognised for many years and a number of innovative numerical schemes have been employed to solve large-scale problems. For example, Deist et al. (1972) introduced the then novel concept of far field influence "lumping" to reduce the time taken for the repeated calculation of remote influence values. The so-called lumping technique can be classified as a "tree method" in which a "quad-tree" structure (see Pfalzner and Gibbon 1996) is introduced to reduce the calculation time for evaluating long-range stress influences at a given collocation point from $O\left(N^2\right)$ to $O(N)$ operations, where N represents the number of discontinuity collocation points. In the case of a planar mine layout problem a square lump mesh with a minimum grid size $G_{\min}$ is superimposed over the problem region. An embedded sequence of lump mesh sizes is then superimposed on the lowest lump mesh grid with the mesh size at level $L \geq 1$ defined to be $G_L = 2^{L-1} G_{\min}$. Influence values are calculated between receiving and sending lump pairs starting at the coarsest lump level $L = L_{\max}$ and are then accumulated at successively finer lump levels as outlined by Napier and Malan (2007). The main parameter controlling the accuracy and efficiency of this procedure is the minimum lump size $G_{\min}$. For a problem comprising N elements covering an area A, the average element grid size is $\overline{g} = \sqrt{A/N}$ and it is usually suitable to set $G_{\min}/\overline{g} \approx 5$ to 10. The main caveat to the

success of the quad-tree scheme is that the average element size should be relatively uniform.

3 Hierarchical Problem Solutions

An extension of the lumping approach outlined above is to obtain the solution of a large-scale layout problem using a hierarchy of solution grid scales which are solved independently in a sequence of steps. In the simplest case the problem is solved at two scales in which the overall layout region is represented using a coarse grid mesh which covers one or more fine scale sub-regions of interest. Each fine scale region is analysed subsequently using appropriate fine scale grid tessellations. This method is akin to the well-known multigrid approach (see, for example, Iserles 1996) but avoids constructing a fine scale solution at all positions within the entire solution domain. In addition, it is evident that the quad-tree "lumping" method can be applied independently at each solution scale using an appropriate lump grid size $G_{\min}$ for each problem scale.

The following sequence of processing steps for a two-scale analysis is then suggested:

Solution procedure—Part I:

(1) Construct a coarse scale mesh representation of the overall layout surrounding one or more given regions of interest. Each region of interest is assumed implicitly to be much smaller than the overall coarse mesh region and should have border edges that are compatible with the neighbouring coarse-scale mesh edges. The coarse-scale mesh must cover each region of interest. (Reference can be made, for example, to the mesh configuration shown in Fig. 4 indicating the initial coarse mesh in a circular excavation with the designated fine scale region occupying the first quadrant in the diagram.)

(2) Solve the coarse-scale layout problem. This solution may be obtained by specifying appropriate lump mesh parameters in which the minimum lump size $G_{\min}$ is not less than five times the average coarse grid mesh size, $\overline{g}$. (The average mesh size is given nominally by $\overline{g} = \sqrt{A/N}$, where A is the area covered by the grid element tessellations and N is the total number of coarse grid elements.)

(3) Load the fine scale element definitions for one or more particular regions of interest.

(4) Calculate the background stress field within each fine-grid region using the coarse-grid element solution values that exist outside each selected fine-grid region. Save the background field stress values in a specified storage file.

Solution procedure—Part II:

(1) Set appropriate lump parameters in a selected fine scale region of interest and load the fine scale element mesh

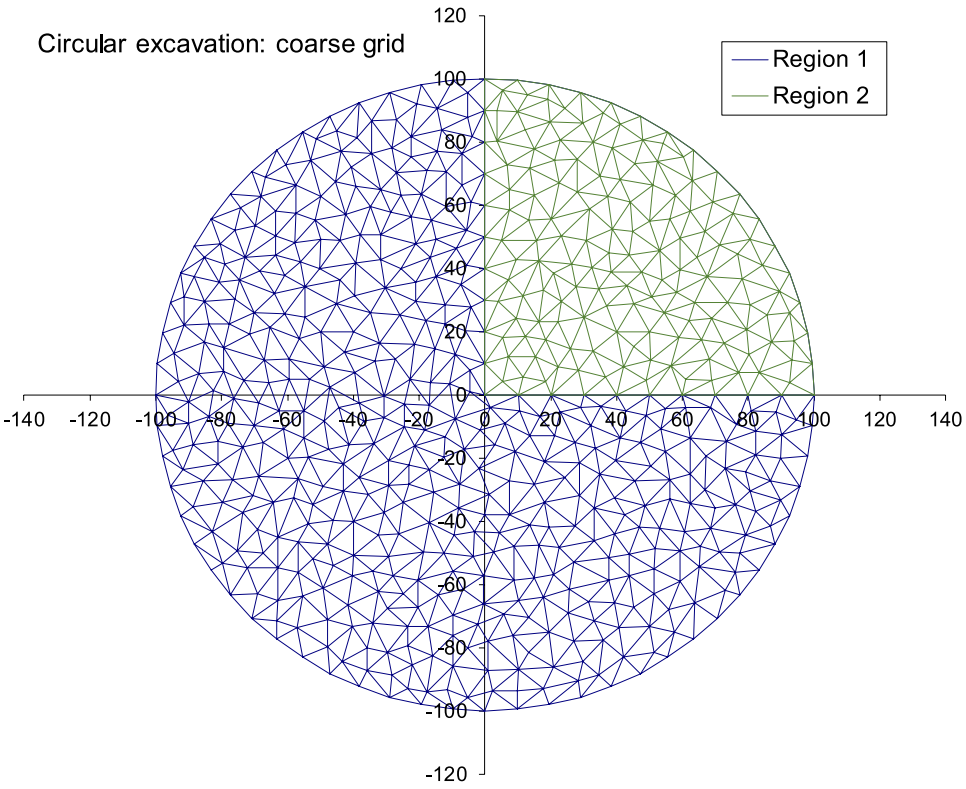

Fig. 4 Coarse grid mesh covering a circular excavation. Region 1 and Region 2 are tessellated with 868 and 296 triangular elements, respectively. The overall mesh area is 31,365.5 m^2 and the average mesh size is $\overline{g}$= 5.191 m. Note that the nominal mesh area is slightly smaller than the theoretical circular area of 31,415.9 m^2

definitions. The $G_{\min}$ parameter in this case is determined by the average fine grid element mesh size.

(2) Load the background field stress values from the saved storage file computed in Part I.

(3) Solve the fine scale problem including mining steps and, if required, a specified number of strength decay time steps within each mining step.

Additional solution refinement—Part III:

(1) If necessary, the solution sequence described above in Part I and Part II can be repeated following suitable remeshing in a selected fine scale region, where a number of mining steps have altered the initial layout edge positions significantly.

The main errors arising in performing the coarse to fine solution transition occur in the fine-scale elements neighbouring the coarse-scale region. These errors can be bounded using high order shape functions for the coarse mesh displacement discontinuity vectors. To illustrate this effect consider an artificial circular excavation with a radius of 100 m and covered with the coarse triangular element mesh, as shown in Fig. 4. The total number of coarse elements is 1164 and the nominal average element grid size is $g = 5.191$ m. Region 2 is delineated as the fine grid "region of interest" which is to be analysed subsequently using a fine scale mesh comprising 1184 elements with an average triangular element grid size of $g = 2.573$ m, as shown in Fig. 5.

The analytic solution for the normal component of elastic convergence, D_z, between the roof and floor of the excavation for a circular excavation with a radius a centred at the origin of the x–y plane is given as a function of the distance r from the origin by

$$D_z = D_z^0 \left[1 - \left(\frac{r}{a}\right)^2\right]^{\frac{1}{2}}, \tag{2}$$

where

$$D_z^0 = \frac{8\sigma_z^P\left(1-\nu^2\right)}{\pi E_m} \tag{3}$$

is the normal component of elastic convergence at the excavation centre, $r = 0$, σ_z^P is the primitive compressive stress field value normal to the excavation plane, E_m is the rock mass Young's modulus and ν is Poisson's ratio. The average convergence in the circular excavation is given by

$$\overline{D}_z = \frac{2D_z^0}{3} \tag{4}$$

Assuming that $a = 100$ m, $\sigma_z^P = 67.5$ MPa, $E_m = 70{,}000$ MPa and $\nu = 0.2$ yields $D_z^0 = 235.73$ mm, and therefore, $\overline{D}_z = 157.15$ mm.

Figure 6 shows a comparison between the convergence values for all elements calculated in the Part I solution phase and the fine grid convergence values determined in the Part II solution phase. These values are also compared to the analytic

Fig. 5 Fine grid mesh in Region 2. The total number of elements is 1184 and the nominal grid size is $\overline{g} = 2.573$ m

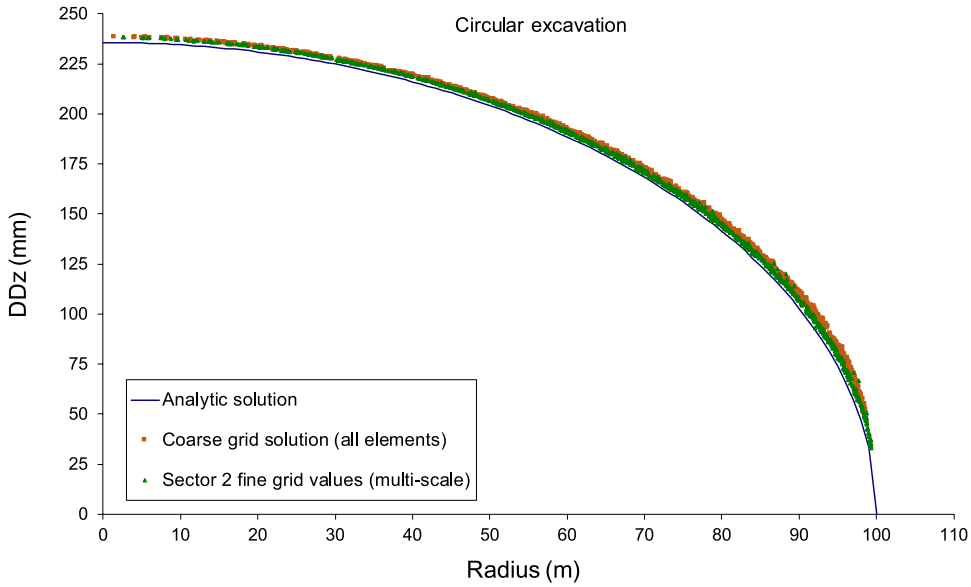

Fig. 6 Comparison of circular excavation multi-scale solutions

solution given by Eq. (1). The numerical solution values follow the analytic solution quite closely, although the coarse solution values are consistently larger than the analytic solution. This is an artefact of the numerical errors that are introduced when using constant displacement discontinuity values in each element. The average convergence value for the coarse element solution was found to be 163.19 mm compared to the analytic solution value of 157.15 mm representing an over-estimation of about 3.8%.

The average convergence value for the fine solution grid using the background stress influence generated by the coarse element solution was calculated to be 161.12 mm giving a satisfactory approximation to the analytic solution with an error of approximately 2.5%. The correction of the solution error introduced by the constant grid can be achieved by the use of high order elements in the coarse grid region or by adapting the local self-effect stiffness influence values in elements that are adjacent to the edge of the excavation (see, for example, Napier and Malan 2007). This adjustment becomes more complicated if the excavation edge fracture zone is modelled explicitly.

4 Shaft Pillar Extraction Example

A large-scale layout problem relating to the extraction of a deep gold mine shaft pillar configuration (Jooste et al. 2023) is shown in Fig. 7 (a simplification of the layout shown in Sect. 7). A specific region of interest for detailed analysis is highlighted in Fig. 7. The overall layout was assumed initially to be horizontal and located at a depth of 2500 m. The primitive field stress at the layout horizon was assigned a value, $\sigma_z^P = 67.5$ MPa, assuming a vertical stress gradient of 0.027 MPa/m. The mined layout region excluding internal remnants and pillars covers an area of approximately 240,310 m^2 and was tessellated using an unstructured triangular element mesh comprising 7082 elements. The nominal average element grid size is $\overline{g} \approx 5.83$ m.

Figure 8 shows an expanded view of the element mesh in the selected region of interest marked in Fig. 7. This diagram shows the currently mined region triangular element mesh edges together with a planned sequence of four mining steps. Each mining step is envisaged to be advanced by 1.5 m over a nominal panel length mining front of 25 m. An initial analysis was carried out with no mining taking place in the mining step region. Three cases were considered.

Case A: The entire layout was analysed using high order cubic element shape functions for the elastic convergence distribution component D_z within each mined triangular mesh element. The discontinuity component variation in each element can be expressed as a cubic polynomial in a local coordinate system with the origin at each element centre as

$$D_z(x,y) = c_0 + c_1 x + c_2 y + c_3 x^2 + c_4 xy + c_5 y^2 + c_6 x^3 + c_7 x^2 y + c_8 xy^2 + c_9 y^3 \quad (5)$$

The coefficients c_k, $k = 0$ to 9 are determined by the calculated discontinuity values at ten assigned internal collocation point positions in each element, as illustrated in Fig. 8. The layout solution in this case comprises a total of 70,820 collocation points, where the elastic convergence discontinuity values are to be calculated. The solution was determined iteratively using a lumped solution scheme with the minimum lump size, $G_{\min} = 40$ m. The explicit solution time for this step was 11,367 s for the desk-top computer that was employed. (The actual run time is quoted to provide an indication of the relative computational costs of the calculation steps. These times will clearly vary depending

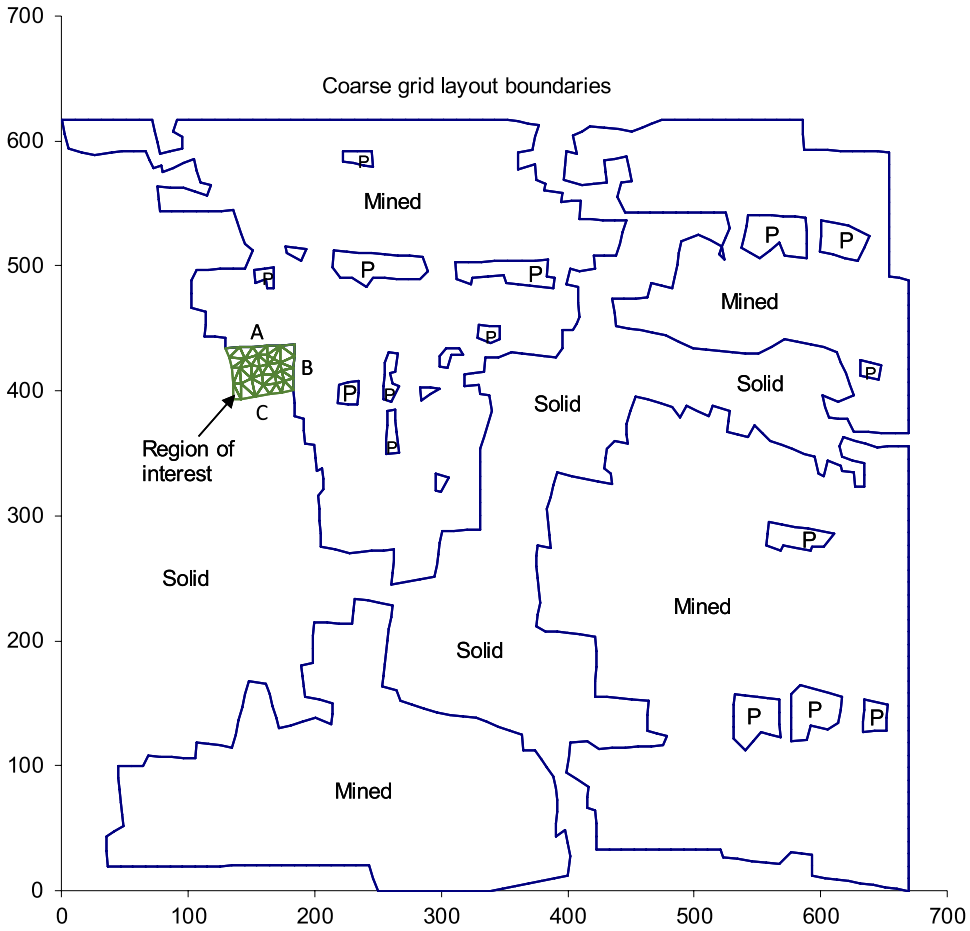

Fig. 7 Overall mine layout showing existing mined regions surrounding a designated region of interest

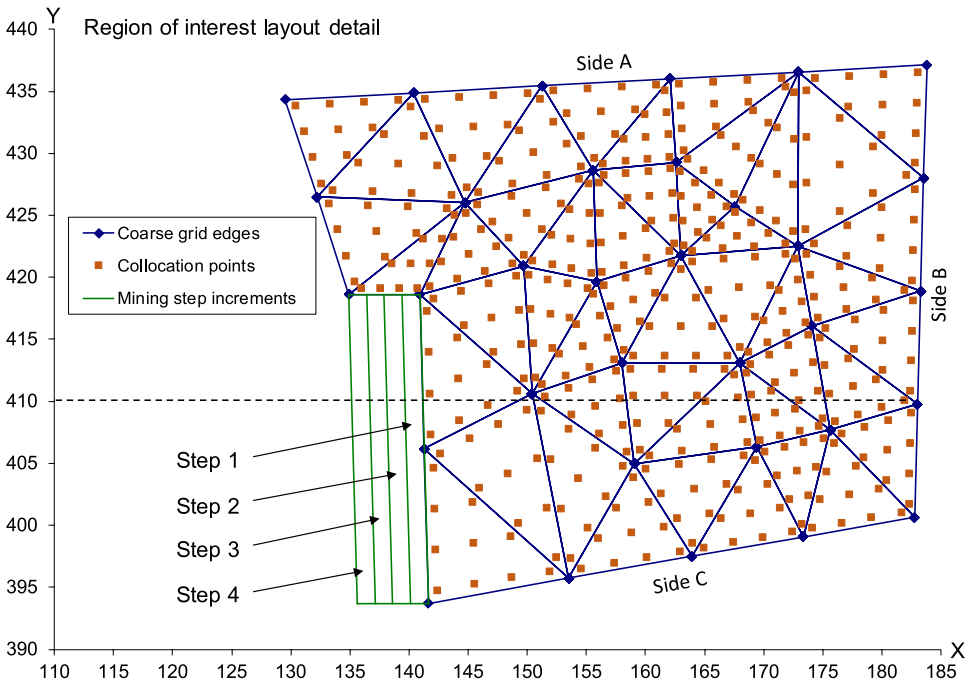

Fig. 8 Expanded view of the coarse mesh in the region of interest shown in Fig. 7 illustrating the collocation point positions of mined and solid elements. The mining step regions designated as Step 1, Step 2, Step 3 and Step 4 are initially solid and the remaining region is mined. (The line $Y=410$ is marked by the dotted line for reference.). The labels A, B and C on the sides refer to the labels in Fig. 7

on the actual hardware configuration that is employed but are quoted to provide a rough indication of the relative computational costs.)

Case B. The layout was analysed in two solution steps using the proposed hierarchical procedure. The solution for the first coarse level step was assumed to be the same as the solution determined in Case A and was used to calculate the effective background stress induced at the centre of each fine scale element. The solution grid in the fine scale region of interest (see Fig. 8) comprised an unstructured triangular element mesh of 19,942 triangular elements. The average grid size in this case was $\overline{g} \approx 0.298$ m and the displacement discontinuity D_z values were assumed to be constant within each element. The fine scale solution step was calculated assuming a lump grid size parameter $G_{\min} = 3.0$ m. The total run time for the fine scale solution step was 7338 s.

Case C. The background solution procedure outlined for Case A was replaced using a coarse triangular element mesh comprising 7082 constant displacement discontinuity elements with a single collocation point at the centre of each element. The run time for the coarse solution step with the number of unknown values reduced from 70,820 to 7082 was 1187 s. The second solution step was repeated as described in Case B using the background stress values induced by the constant coarse mesh solution at the centres of the 19,942 fine mesh elements also assuming a lump grid size parameter $G_{\min} = 3.0$ m. (The run time in this case was 7161 s and is nominally the same as for the Case B fine element solution.)

The reduction in calculation time is significant, since it is typically required to perform multiple scenario investigations when planning a proposed excavation sequence in a given mining region. In the present case these can involve the analysis of multiple mining steps with multiple time steps in each excavation increment to represent time-dependent face crushing effects. The cited time reductions for the individual analyses can, therefore, be considered to be multiplied by factors of 10–100 for each excavation sequence scenario that is planned for a mining extraction sequence that may last for several months in real time.

Figure 9 shows a comparative plot of the reef-normal elastic convergence values for the three selected cases. The results are plotted in the x-coordinate direction across the region of interest for the selected y-coordinate value of 410 m (see Fig. 8). The convergence value at each point is interpolated from the local covering element shape function. For the higher order elements in Case A the shape function is given by Eq. (5) but is constant in the fine element mesh that is used in Case B and Case C. It is clear that there is a very close agreement between the high order cubic polynomial element solution values generated in Case A and the two-stage solution obtained in Case B. This result is extremely important and demonstrates the effectiveness of the high order coarse element solution in allowing accurate background stress values to be calculated for the fine element solution. The solution values obtained in Case C indicate that the background stress values determined by the constant coarse element background solution are significantly over-estimated near the interface between the coarse and fine mesh regions.

It is important to note that the motivation for using the fine mesh in a given region of interest is dictated by both the geometric complexity of the layout configuration in specific cases and by the requirement to provide an accurate solution resolution for the stress distribution in the fracture zone ahead of the stope face (Napier and Malan 2018). This resolution is required as well to perform a detailed analysis of the time-dependent evolution of the

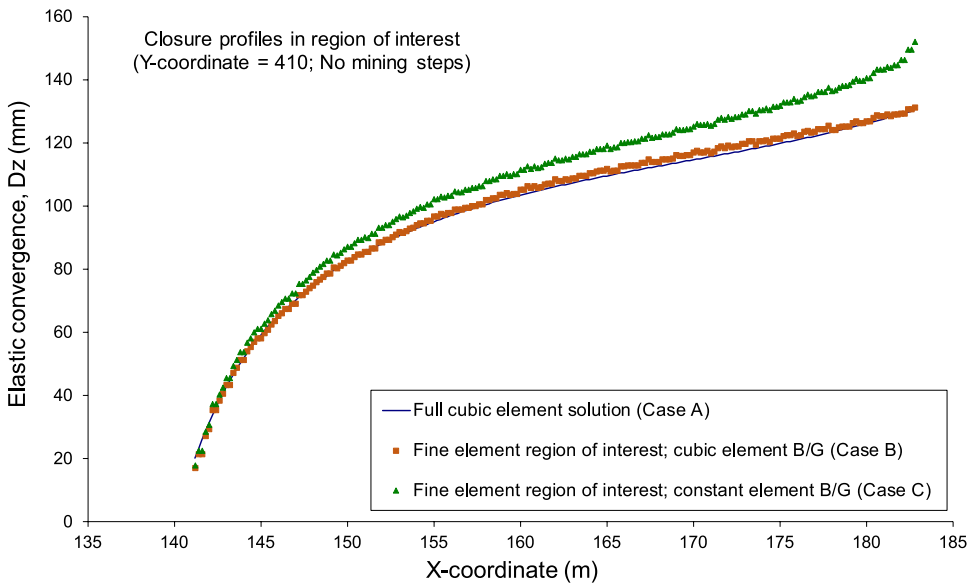

Fig. 9 Comparison plots of closure profiles between the three selected cases A, B and C used to evaluate the accuracy and performance of the proposed two-stage solution procedure

fracture zone stress distribution and peak stress values in the rock mass in front of the excavation edges. This evaluation can be expedited further by employing a partitioning scheme in the influence matrix that is formulated for a fine scale region of interest as described in the next section.

5 Partitioned Influence Matrix Formulation

In determining repetitive solutions in a given region of interest it may be advantageous to partition the collocation points in the region into a set A having N_A collocation points and a set B having N_B collocation points, where the total number of points is $N = N_A + N_B$. In addition, the two partitions are selected to include all points having non-linear boundary conditions in region A and to ensure that all points in region B have fixed traction boundary conditions (specifically zero traction on the surface of an open excavation point) or fixed total closure conditions. Symbolically, Eq. (1) can be rewritten in the partitioned matrix form as

$$\begin{bmatrix} T_A \\ T_B \end{bmatrix} = \begin{bmatrix} K_{AA} & K_{AB} \\ K_{BA} & K_{BB} \end{bmatrix} \begin{bmatrix} D_A \\ D_B \end{bmatrix} + \begin{bmatrix} E_A \\ E_B \end{bmatrix}, \tag{6}$$

where T_A and D_A are, respectively, the traction vector and the displacement discontinuity vector components in region A and where, similarly, T_B and D_B are the traction vector and the displacement discontinuity vector components in region B. The subscripts R and S assigned to each sub-matrix K_{RS} in Eq. (6) represent the respective receiving and sending point regions. The vectors E_A and E_B represent existing field stress values combined with any externally calculated background stress values.

Assuming that $T_B = 0$ in region B, the second row of Eq. (6) becomes

$$K_{BA}D_A + K_{BB}D_B + E_B = 0 \tag{7}$$

Defining K_{BB}^{-1} as the inverse of matrix K_{BB}, Eq. (7) can be solved for D_B in the form:

$$D_B = -K_{BB}^{-1}\left(K_{BA}D_A + E_B\right) \tag{8}$$

Substituting Eq. (8) into the first row of Eq. (6) provides the relationship:

$$T_A = \hat{K}_{AA}D_A - \hat{K}_{AB}E_B + E_A \tag{9}$$

where

$$\hat{K}_{AA} = K_{AA} - K_{AB}K_{BB}^{-1}K_{BA} \tag{10}$$

and

$$\hat{K}_{AB} = K_{AB}K_{BB}^{-1} \tag{11}$$

Equation (9) can be solved iteratively as a reduced system having $3N_A$ equations for the displacement discontinuity values D_A provided the inverse matrix K_{BB}^{-1} can be determined. This represents a reduction in the unknown displacement discontinuity values from $3\left(N_A + N_B\right)$ in Eq. (6). The number of equations in the set (9) is reduced further from $3N_A$ to N_A in the special case, where only the excavation–normal convergence is required. The reduced equation system (9) effectively incorporates the presence of the open excavation region B and the solution speed is consequently expedited if all the matrix components in Eqs. (10) and (11) are precalculated and stored in memory. The displacement discontinuity components D_B in region B can be recovered from Eq. (8) following the solution of Eq. (9) for D_A.

The main drawback of this scheme is the necessity to calculate the inverse matrix K_{BB}^{-1}. The inverse matrix can be evaluated; however, using a standard singular value decomposition algorithm (see Press et al. 1992) provided the order of the matrix, K_{BB} is less than approximately 4000–5000. Alternative inverse matrix approximation techniques for larger scale systems can be investigated if necessary. In special cases such as two-dimensional plane problems, a number of analytic solutions are also available. The partitioning concept is related as well to the suggested boundary integral equation solution strategy presented previously by Martin and Rizzo (1995).

The partitioned influence scheme can be combined effectively with the hierarchical solution approach in which the external traction influence vectors E_A and E_B include the coarse background solution values. The overall procedure requires the solution of the coarse grid layout representation and the transfer of the coarse influence values to the fine-scale regions of interest as discussed in the previous section. In certain cases, it may be possible as well to represent parts of the fine-scale solution region using high order displacement discontinuity element shape functions. This approach is illustrated in the following section.

6 Illustrative Application of the Partitioned Influence Matrix Scheme

Figure 8 shows the detailed mesh configuration of the selected region of interest together with four possible mining step increments adjacent to the mined region which is covered with high order triangular displacement discontinuity elements. (The multiple collocation points shown in Fig. 8 define a polynomial shape function in each mined element given by Eq. (5).) The total number of coarse grid elements in Fig. 8 is 46 with 460 internal collocation point positions. The mining step region is tessellated with 420 fine grid constant elements in each potential incremental step region 1–4. The total number of collocation points in

the region of interest is, therefore, $4 \times 420 + 460 = 2140$. The background stress was computed as described previously at each of these collocation points using the results determined in Case A above.

To demonstrate the partitioning scheme a solution is obtained for the simplified case, where only the Step 1 region is mined and the fracture zone extent in the combined area covering Step2, Step 3 and Step 4 is calculated using the limit equilibrium model described by Napier and Malan (2018).

The following element partition regions are defined for this analysis.

Partition region *A*: This partition comprises the combined region covering the three mining step regions 2, 3 and 4 that are designated in Fig. 8 and includes $3 \times 420 = 1260$ collocation points. The selected elements are assumed to have the following crush element constitutive properties which are summarised in Table 1.

In the case of a plane strain stress state parallel to a straight excavation edge, the simple crush zone limit model implies that the distribution of the reef-normal vertical stress at a distance x from the excavation edge in the reef plane given by

$$\frac{\sigma_n}{\sigma_c} = e^{\frac{2m\tan\phi_I x}{H}}, \tag{12}$$

where

$$m = \frac{\left(1 + \sin\phi_I\right)}{\left(1 - \sin\phi_I\right)} \tag{13}$$

Partition region *B*: This partition includes the Step 1 region of 420 mined elements which are immediately adjacent to the 46 high order elements shown in Fig. 8. The total number of collocation points in partition region *B* is, therefore, $420 + 460 = 880$. All elements in the partition region *B* are fully mined with a zero stress boundary condition applied at each collocation point.

The partitioned matrix region results were compared to the equivalent analysis of the region 1 area of interest (see Fig. 8 and Case B) analysed using a fine grid mesh with $19{,}942 + 1280 = 21{,}622$ uniformly sized elements with a single collocation point in each element. This problem was solved using a lumping scheme with three lump levels and a minimum lump size of 2.0 m. The solution time for the fine grid was 3414 s in this case and the average convergence in the mined region excluding the mining step regions was 120.41 mm. The corresponding partitioned element solution time was 100 s and the average convergence in the mined region was 116.41 mm. This clearly represents a very significant reduction in the computational cost that would be incurred in processing multiple time step increments in which the rock strength is prescribed to decay at a specified rate following a mining step increment. It is also of interest to note that the solution time is only increased to 352 s if the partitioning scheme is not used in this case, again emphasizing the utility of employing the high order element shapes in the local region of interest shown in Fig. 8.

A comparison between the average convergence values and the average reef-normal traction values for the fine grid and partitioned matrix solutions within each of the four mining step regions is summarised in Table 2. The results are very similar, although the high order element scheme convergence values are slightly lower than the corresponding values for the full fine grid solution. A further comparison between the closure values obtained for the fine grid analysis and the values obtained from the partitioned influence matrix solution is given in Fig. 10. This plot confirms that the partitioned matrix convergence values are slightly lower than the corresponding fine mesh values in partition region B but are in close agreement in the mining step zone within partition region A. Figure 11 illustrates a comparison between the vertical stress component values in the crush zone elements falling in partition A for the partitioned matrix solution and the fine grid solution. The analytic crush zone reef-normal stress profile for the plane strain stress state given by Eq. (12) is also superimposed on this plot for comparison.

Table 1 Crush zone model parameters

Parameter	Value
Crush zone interface friction angle and crushed rock internal friction angle, ϕ_I	30°
Crush zone uniaxial strength, σ_c	100 MPa
Crush zone height, H	3.0 m

Table 2 Comparison between fine element solution and partitioned matrix solution values in the mining step element regions

Mining step region	Fine element solution		Partitioned matrix solution	
	Convergence (mm)	Vertical stress (MPa)	Convergence (mm)	Vertical stress (MPa)
Step 01	36.60	0.0	34.79	0.0
Step 02	13.78	− 278.79	12.41	− 279.39
Step 03	4.48	− 241.22	3.68	− 239.18
Step 04	2.57	− 171.03	2.14	− 167.15

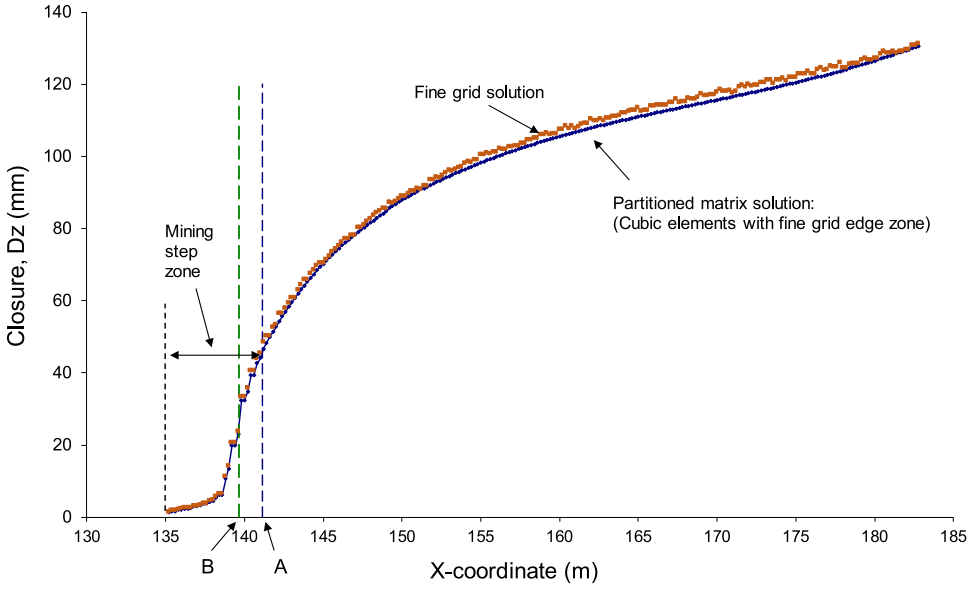

Fig. 10 Comparison between the convergence values for the fine grid solution and the partitioned matrix collocation points along a horizontal section having *Y*-coordinate 410 (see Fig. 8)

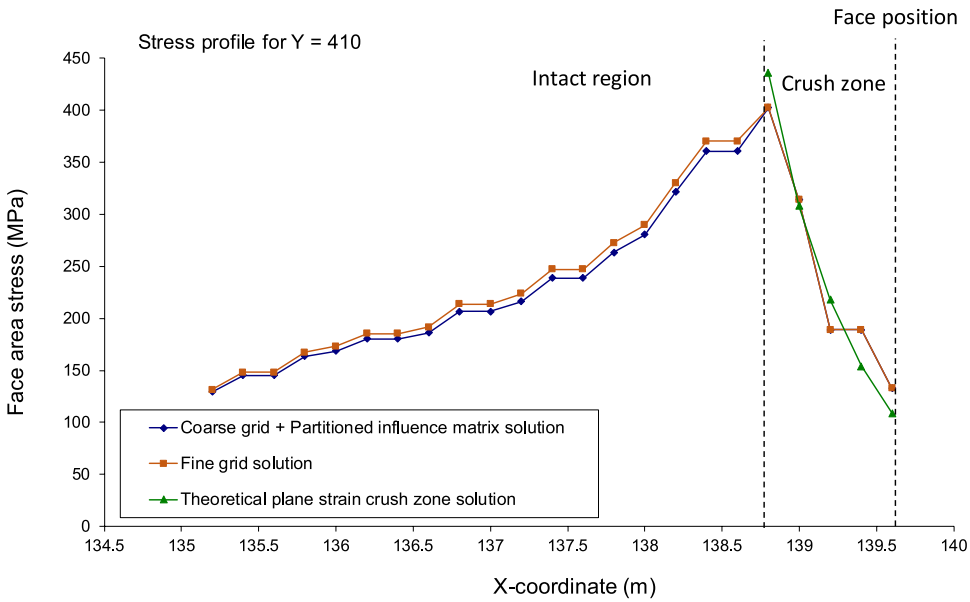

Fig. 11 Comparison between the vertical stress values in the crush zone region of the fine grid solution and the partitioned matrix collocation points along a horizontal section having *Y*-coordinate 410 (see Fig. 8)

The peak stress and the stress values in the intact zone ahead of the peak stress show close agreement, although the partitioned matrix vertical stress magnitude results are slightly smaller than the fine element solution values. (It should be noted that the crush zone region is on the right hand side of the peak stress in Fig. 11. The decreasing stress in the unfractured region is to the left of the peak stress position shown in Fig. 11.)

7 Practical Application of the Multi-scale Method to Simulate Stope Convergence

Jooste et al. (2023) described a combined bulking and limit equilibrium model to simulate the stope convergence at a particular location when mining a shaft pillar (the Bambanani Shaft pillar shown in Fig. 12). Note that both the bulking and limit equilibrium model include a time dependent component (see Jooste et al 2023 and Napier and Malan 2018). To allow for time-dependent bulking in the back areas of the mined region, it is postulated that the bulking parameter follows a time dependent evolution between a specified initial value and maximum value. For the limit

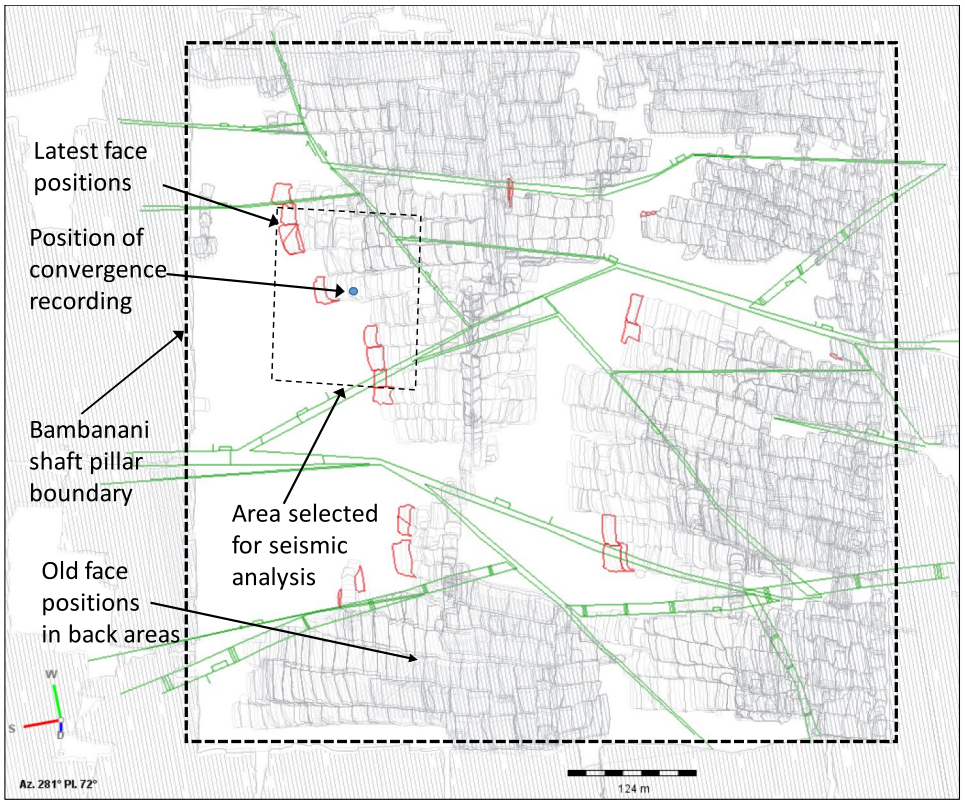

Fig. 12 Mining outlines in the Bambabanani Shaft pillar. These were the final stope face positions when the mining was abandoned in the pillar. The position of the convergence logger is indicated by the blue dot (Color figure online)

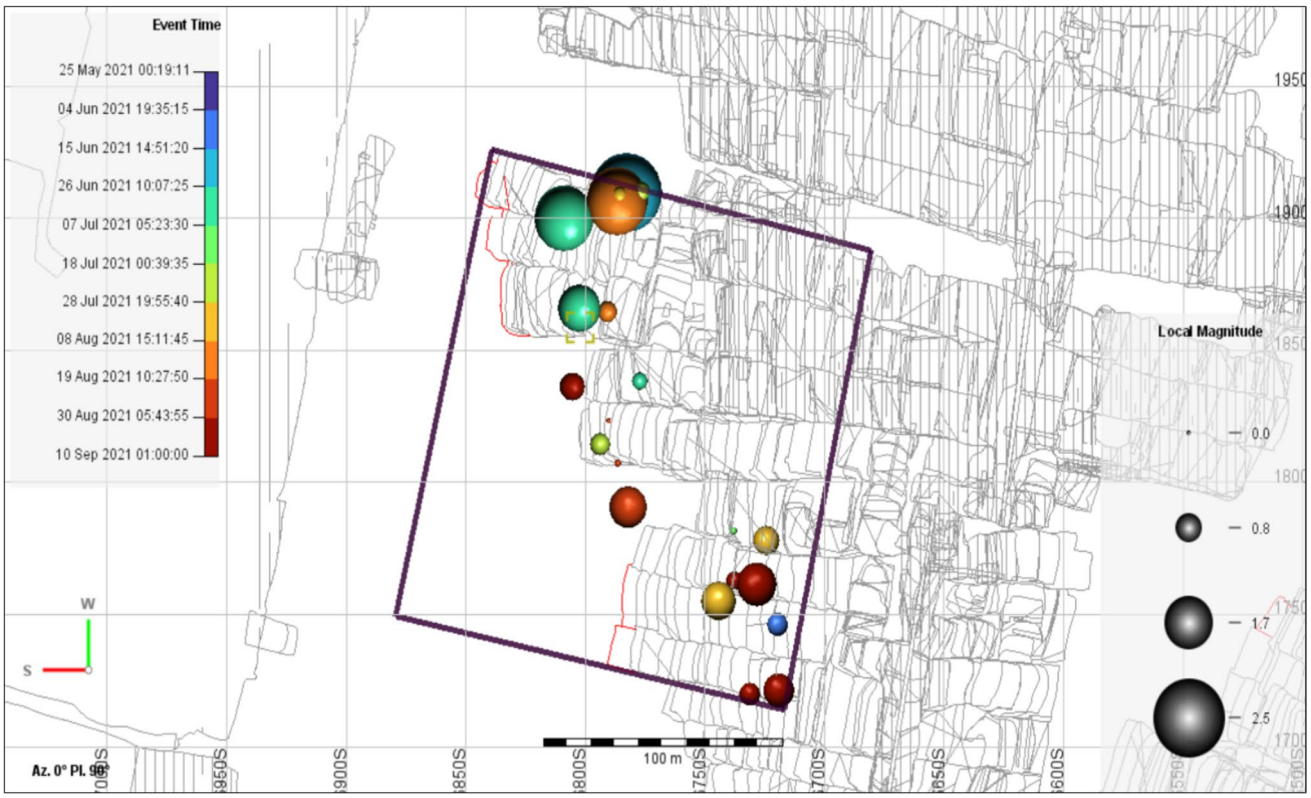

Fig. 13 Seismic events of local magnitude ≥ 0.0 recorded in close proximity to the panel, where the convergence was recorded for the period from 25 May 2021 to 9 September 2021

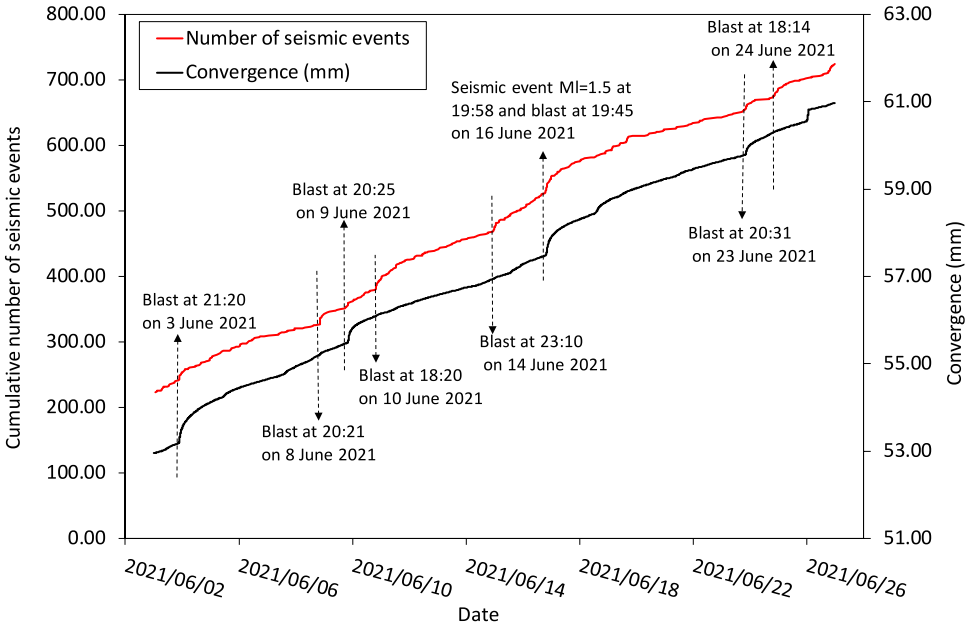

Fig. 14 Stope convergence at the position indicated in Fig. 12 and the number of seismic events recorded in the area around this measurement position (polygon shown in Figs. 12 and 13)

equilibrium model, the strength of the intact rock is defined by an unconfined strength value and by a slope parameter. Once the material has failed, the strength is assumed to decay to a residual strength envelope according to a simple exponential decay function.

An example of the seismicity and recorded time-dependent panel convergence in the region of interest is shown in Figs. 13 and 14, respectively. The convergence profile is similar to the results reported by Malan (1999) and Malan et al. (2007). It is of interest to note the significant time-dependent convergence and the jumps in convergence that occur during successive blasting events, as shown in Fig. 14. The constitutive model used by Jooste et al. (2023) for the modelling employs a specified parameter (the so-called bulking factor) to inflate the magnitude of the simulated elastic convergence in the excavated region. The model also specifies an assumed compaction function to simulate the stress recovery rate following contact between the roof and floor of the mined back area regions. Specific details of the model are given in Jooste et al. (2023). The original work was computationally intensive, as only a fine mesh was used for the entire model. Jooste et al. (2023) noted that, "*Small element sizes were required for the limit equilibrium model, and therefore, it was not feasible to simulate the entire shaft pillar geometry*".

As described above, the simulation of time-dependent stope convergence is carried out by postulating that the rock strength ahead of the mining face is described by either a Mohr–Coulomb failure criterion in which the strength parameters decay exponentially once the intact strength is exceeded. In this case it is necessary to calculate the time-dependent reef-parallel confining stress at all positions ahead of the mining face to track the moving fracture zone edge position. A special "fast marching" technique is used to perform these calculations as part of the iterative solution. A detailed explanation of this procedure is given by Napier and Malan (2018). Additional simulation procedures to represent the back area time-dependent convergence and stress recovery have been described in Jooste et al (2023). This present section extends this earlier work using the hierarchical solution method described in Sect. 3 of the current paper. The coarse and fine mesh used is shown in Fig. 15. It was found that the parameters shown in Table 3 gave reasonable results, although further work on calibrating the model is required.

The simulated convergence profiles are shown in Fig. 16 as a function of time in the area of interest for three mining increments. The convergence was calculated in the centre of the panel (see Fig. 17) at different distances from the face. The simulated results are qualitatively similar to the underground observations and it is noted that the magnitude of the convergence decreases as a function of distance to face (Malan 1999). This is caused by the tabular nature of these excavations. The jumps in convergence at blasting time also become smaller as this distance increases. For the convergence observation point that was initially 10 m from the face, the total increase in convergence during this period was 63 mm. This is much larger than typically recorded in the Bambanani Shaft pillar and additional simulations were carried out to check this. It is evident that the overall increase in the convergence can be reduced using a smaller bulking factor. However, precisely accurate calibration using the actual convergence data presented in Fig. 14 is difficult as insufficient observations are available concerning the actual

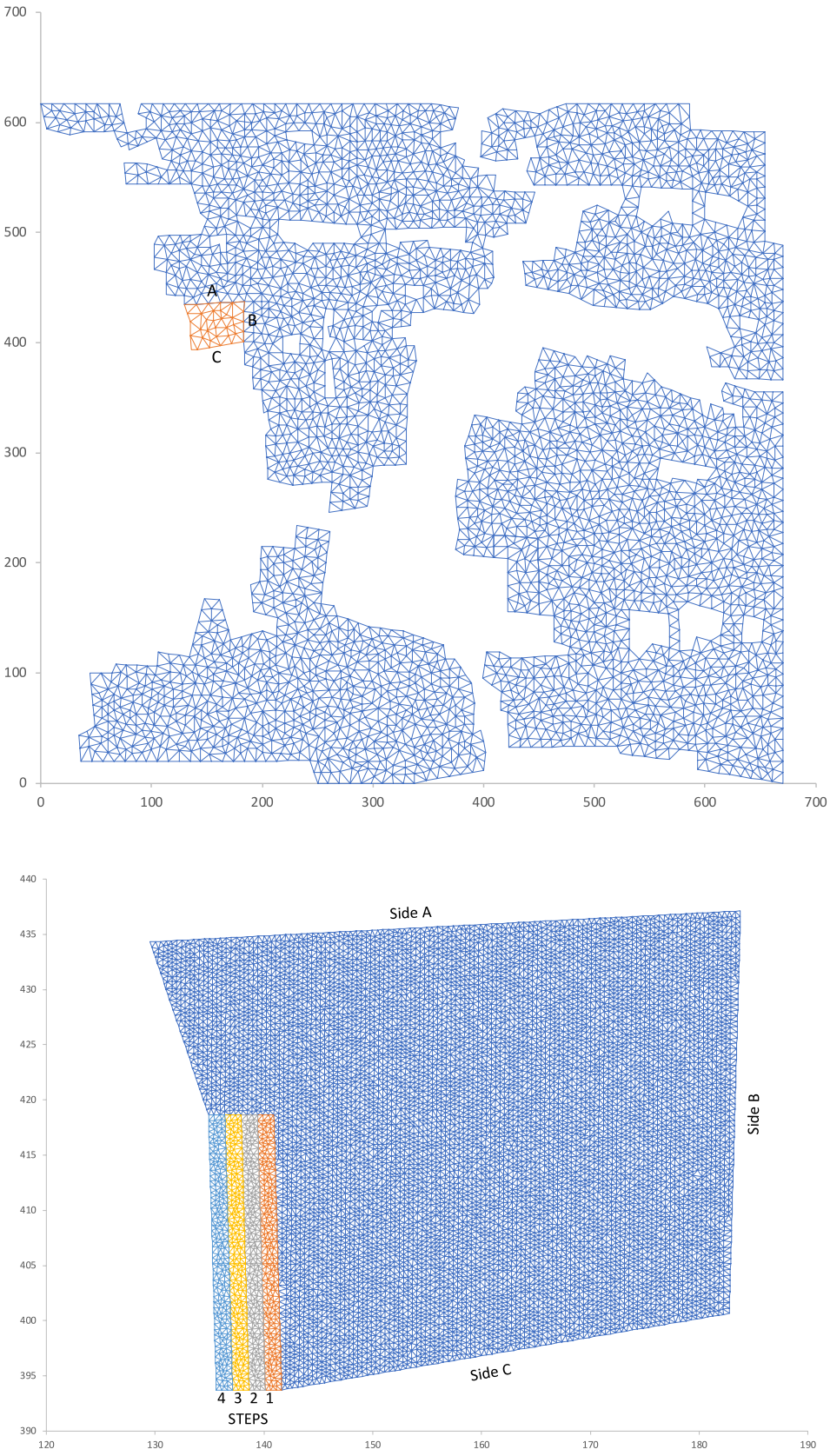

Fig. 15 Coarse and fine mesh in the area of interest. The labels A, B, and C are used to indicate the position of the fine mesh relative to the coarse mesh

Table 3 Parameters used for the geometry, the bulking model and the limit equilibrium model

Parameter	Value
Depth	2500 m
Face advance increment	1.5 m
Dip	0°
Young's modulus, E	70 GPa
Poisson's ratio, ν	0.2
Number of elements in the coarse mesh	7088
Number of elements in the fine mesh	21,622
Average grid size—coarse mesh, $\overline{g}$	≈ 34 m^2
Average grid size—fine mesh, $\overline{g}$	≈ 0.089 m^2
Intact strength intercept, σ_c^i	150 MPa
Intact strength slope, m_i	3
Initial residual strength intercept, σ_c^0	150 MPa
Initial residual strength slope, m_0	3
Final residual strength intercept, σ_c^f	15 MPa
Final residual strength slope, m_f	3
Effective mining height, H	1.5 m
Intact seam stiffness modulus, k_s	46 667 MPa/m
Fracture zone interface friction angle, ϕ	35°
Limit equilibrium half-life parameter, λ	0.5 h
Initial bulking factor, B_f^0	2
Final bulking factor, B_f^m	2.5
Bulking half-life parameter, λ_B	28.9 h
Compaction stiffness, E_0	10 000 MPa

The limit equilibrium parameters are defined in Napier and Malan (2018) and the bulking parameters in Jooste et al (2023)

face advance per blast, a lack of detailed knowledge of the blasting sequence of neighbouring faces and no precise records of the accompanying seismic activity. The qualitative results depicted in Fig. 16 are nevertheless encouraging and illustrate the effect of the distance from the convergence meter to the mining face on the convergence profiles. The convergence increments at blasting time decrease as mining proceeds and the distance to the mining face increases.

The detailed abutment locations relative to the convergence measuring points also affect the simulated and observed convergence profiles. This is demonstrated by considering the three measurement points shown in Fig. 17. The convergence at Position 3, which is close to the lower abutment, is substantially lower than the other convergence profiles. The time-dependent convergence between blasts is seen as well to be different for the three selected measuring positions. This may possibly explain the variability typically seen when recording panel convergence data and further complicates the calibration process of the numerical model. It is clear that accurate records of the positions of the convergence loggers need to be kept when conducting underground measurements and the precise layout configuration of the panels needs to be accurately represented.

In summary, encouraging results were obtained with the proposed new methodology to simulate the time-dependent rock mass behaviour of a very deep tabular excavation. These results are considered to be a first-order approximation to the inelastic rock mass behaviour near excavation edges and to provide a framework to guide the future development of constitutive descriptions of the fractured rock mass in deep mines.

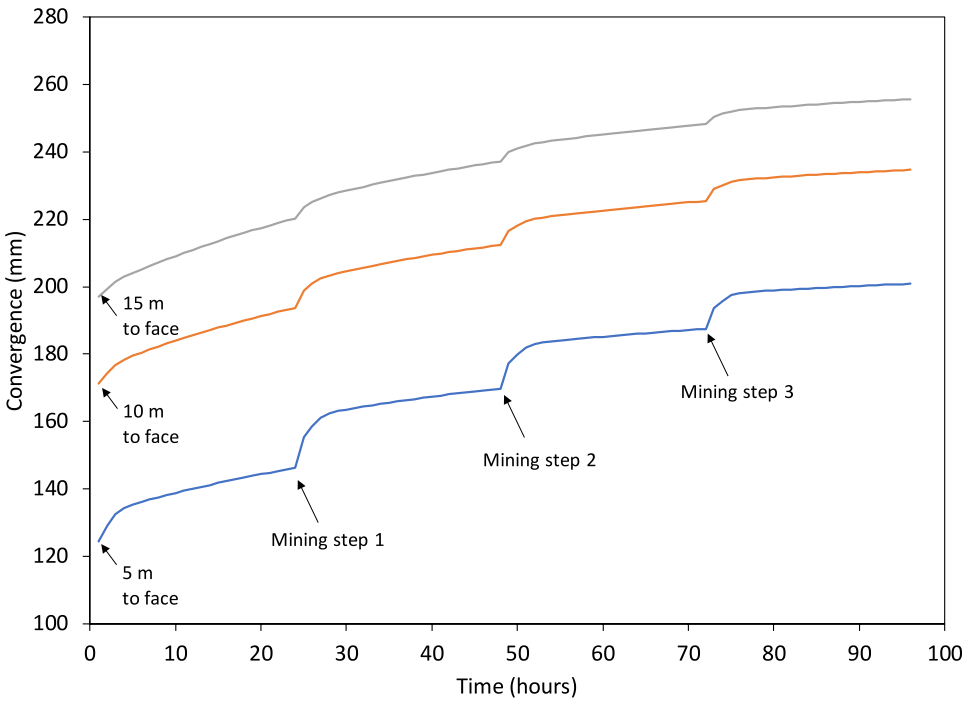

Fig. 16 Simulated convergence profiles for the region of interest. The parameter values in Table 3 were used for these simulations

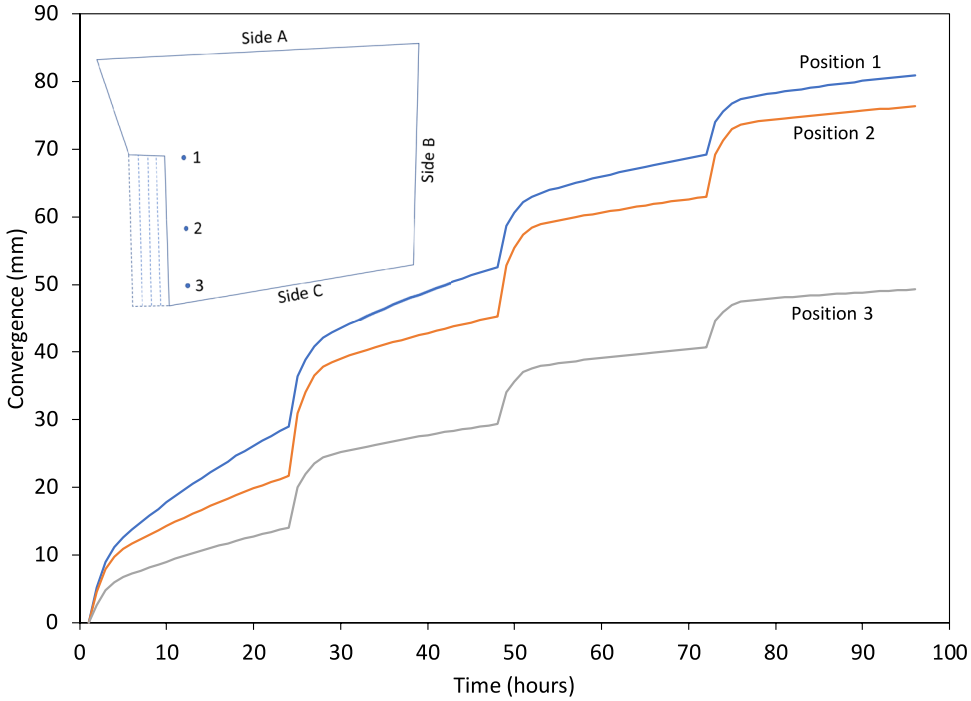

Fig. 17 Simulated convergence profiles for different positions in the panel. Position 3 was against the solid abutment and Position 1 was adjacent to the mined panel (also see Fig. 15)

The modelling methodology and constitutive codes are difficult to calibrate and represent a universal challenge for the application of rock engineering numerical models. As more complex numerical models are developed for the improved simulation of observed rock mass behaviour, more onerous requirements of model calibration and user expertise are required. This not only applies to boundary element models, but also to finite element and finite difference codes. Elmo et al (2022) made the following important observation: "*It is evident generally that if older and simpler solutions have a clear advantage in terms of durability and/or efficiency, even if this advantage is restricted to a limited purpose, they continue to exist and evolve*." It is envisaged that the model described in this paper can be used as a specialised tool to investigate the mechanisms of proposed stope support strategies for different mining rates and to study the effect of mining rate on back area stope closure and face stress stability.

8 Conclusions and Additional Developments

Two approaches have been proposed to allow the simulation of small regions of interest within large-scale extensively mined tabular layouts. In the first method it is shown that a simple two-step hierarchical solution procedure can be readily constructed to allow the efficient calculation of stope convergence values in local small-scale regions of interest. The most significant finding in this case is that the use of high order elements in the coarse solution step can provide a self-consistent representation of the fine region background influence values. It is shown as well that the fine region solution efficiency can be enhanced dramatically by combining higher order elements with fine scale elements in a partitioned influence matrix for the problem solution. The cells in the sub-matrix which is inverted are chosen to correspond to open excavation elements having simple zero stress boundary conditions. This approach enables the size of the core solution influence matrix to be reduced substantially while retaining the appropriate coupling to the zero stress partition region. The reduction of the active influence matrix size enables the efficient simulation of multiple small scale mining increments which may include a sequence of mining steps and time-step increments that are required to simulate rock mass strength decay and creep effects. This increase in computational speed allows the feasible calculation of sequential mining step advances to be combined with multiple time step cycles in the analysis of the evolutionary stress distribution in the fracture zone ahead of each mining face.

A specific case study was analysed using the hierarchical two-step procedure applied to the extraction of a shaft pillar within an extensively mined region. The results of this study show that the fine scale convergence behaviour can be modelled accurately and efficiently without having to incorporate the entire excavation region in the fine scale solution. The study emphasizes that the quantitative calibration of the model requires precise geometric data relating to mine panel outlines and accurate records of exact blast time sequences and the accompanying seismic activity levels.

The hierarchical calculation scheme described in this paper can be extended to address the analysis of pillar mining problems, where the behaviour of a few selected pillars is to be analysed within an extensive layout comprising hundreds of pillars. The approach can be useful as well to investigate the interactions between large underground excavations such as haulages or pump chambers having traction-free surfaces and the non-linear creep behaviour of intersecting fault structures.

Acknowledgements This work was undertaken under the auspices of the Harmony Gold Chair of Rock Engineering, and the authors would like to thank Harmony Gold Mining Company for permission to publish this paper.

Author Contributions J.A.L Napier conceptualized the hierarchical solution scheme and coded this in a displacement discontinuity code. He also conducted preliminary numerical simulations to test the scheme. The collection and analysis of the stope convergence data for the shaft pillar case study was done by Y. Jooste. D.F. Malan and Y. Jooste did the numerical modelling of this case study. All three authors contributed to the writing of the final paper and approved the final manuscript.

Funding Open access funding provided by University of Pretoria. The Chair funded the work described in this paper.

Data availability The authors declare that all the data supporting the findings of this study are available within the article.

Declarations

Conflict of interest The authors have no competing interests to declare that are relevant to the content of this manuscript. Harmony Gold Mining Company Ltd supports the Harmony Gold Chair in Rock Engineering and Numerical Modelling at the University of Pretoria.

References

Adhikary D, Khanal M, Jayasundara C (2016) Deficiencies in 2D simulation: a comparative study of 2D versus 3D simulation of multi-seam longwall mining. Rock Mech Rock Eng 49:2181–2185. https://doi.org/10.1007/s00603-015-0842-7

Berry DS, Sales TW (1962) An elastic treatment of ground movement due to mining—part III. Three dimensional problems, transversely isotropic ground. J Mech Phys Solids 10:73–83. https://doi.org/10.1016/0022-5096(62)90030-3

Crouch SL, Starfield AM (1983) Boundary element methods in solid mechanics. George Allen and Unwin, London

Cundall PA (1987) Distinct element models of rock and soil structure. In: Brown ET (ed) Analytical and computational methods in engineering rock mechanics, Ch. 4. Allen & Unwin, London, pp 129–163

Deist FH, Georgiadis E, Moris JPE (1972) Computer applications in rock mechanics. J S Afr Inst Min Metall 72:265–272

Elmo D, Mitelman A, Yang B (2022) Examining rock engineering knowledge through a philosophical lens. Geosciences 12:174. https://doi.org/10.3390/geosciences12040174

Fuławka K, Stolecki L, Kołodzie R (2025) Application of large-scale finite element method simulations to determine geomechanical hazard during room-and-pillar mining under a tectonic fault. In: AfriRock 2025, Pioneering Progress—the future of rock engineering, 21–23 July 2025. The Southern African Institute of Mining and Metallurgy, Sun City, South Africa, pp 241–252

Gay NC (1979) The state of stress in a large dyke on E.R.P.M., Boksburg, South Africa. Int J Rock Mech Min Sci 16:179–185. https://doi.org/10.1016/0148-9062(79)90483-2

Iserles A (1996) A first course in the numerical analysis of differential equations. Cambridge University Press, New York

Jooste Y, Malan DF (2020) The need for improved layout design criteria for deep tabular stopes. J S Afr Inst Min Metall 120(1):23–32. https://doi.org/10.17159/2411-9717/849/2020

Jooste Y, Napier JAL, Malan DF (2023) A bulking model to simulate stope convergence in deep tabular excavations. Int J Rock Mech Min Sci 170:105480. https://doi.org/10.1016/j.ijrmms.2023.105480

Malan DF (1999) Time-dependent behaviour of deep level tabular excavations in hard rock. Rock Mech Rock Eng 32(2):123–155. https://doi.org/10.1007/s006030050028

Malan D, Napier J (2018a) A limit equilibrium fracture zone model to investigate seismicity in coal mines. Int J Min Sci Technol 28:745–753. https://doi.org/10.1016/j.ijmst.2018.08.003

Malan DF, Napier JAL (2018b) Rockburst support in shallow-dipping tabular stopes at great depth. Int J Rock Mech Min Sci 112:302–312. https://doi.org/10.1016/j.ijrmms.2018.10.026

Malan DF, Napier JAL, Janse van Rensburg AL (2007) Stope deformation measurements as a diagnostic measure of rock behaviour: a decade of research. J S Afr Inst Min Metall 107:743–765

Martin PA, Rizzo FJ (1995) Partitioning boundary integral equations, and exact Green's functions. Int J Numer Methods Eng 38:3483–3495. https://doi.org/10.1002/nme.1620382007

McGarr A, Wiebols GA (1977) Influence of mine geometry and closure volume on seismicity in a deep-level mine. Int J Rock Mech Min Sci 14:139–145. https://doi.org/10.1016/0148-9062(77)90005-5

Napier JAL, Malan DF (2007) The computational analysis of shallow depth tabular mining problems. J S Afr Inst Min Metall 107:725–742

Napier JAL, Malan DF (2018) Simulation of tabular mine face advance rates using a simplified fracture zone model. Int J Rock Mech Min Sci 109:105–114. https://doi.org/10.1016/j.ijrmms.2018.06.024

Pfalzner S, Gibbon P (1996) Many-body tree methods in physics. Cambridge University Press, New York

Plewman RP, Deist FH, Ortlepp WD (1969) The development and application of a digital computer method for the solution of strata control problems. J S Afr Inst Min Metall 70:33–44

Press WH, Teukolsky SA, Vetterling WT, Flannery BP (1992) Numerical recipes in Fortran 77. Cambridge University Press, New York

Ryder JA (1988) Excess shear stress in the assessment of geologically hazardous situations. J S Afr Inst Min Metall 88:27–39

Salamon MDG (1963) Elastic analysis of displacements and stresses induced by the mining of a seam or reef deposit—part I. Fundamental principles and basic solutions as derived from idealized models. J S Afr Inst Min Metall 64:128–149

Wiles TD (2005) Rockburst prediction using numerical modelling—realistic limits for failure prediction accuracy. In: Potvin Y, Hudyma M (eds) RaSiM6 Proceedings of the Sixth International Symposium on Rockburst and Seismicity in Mines Proceedings, Australian Centre for Geomechanics, Perth, pp 57–63